



Universiteit Gent
Faculteit Wetenschappen
Vakgroep Fysica en Sterrenkunde

2 No title yet

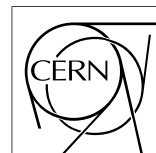
3 No sub-title neither, obviously...

4 Alexis Fagot

5



Thesis to obtain the degree of
Doctor of Philosophy in Physics
Academic years 2012-2017





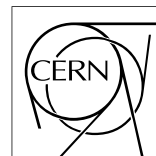
Universiteit Gent
Faculteit Wetenschappen
Vakgroep Fysica en Sterrenkunde

7
8 Promotoren: Dr. Michael Tytgat
Prof. Dr. Dirk Ryckbosch

9
10 Universiteit Gent
11 Faculteit Wetenschappen
12
13 Vakgroep Fysica en Sterrenkunde
14 Proeftuinstraat 86, B-9000 Gent, België
15 Tel.: +32 9 264.65.28
16 Fax.: +32 9 264.66.97



Thesis to obtain the degree of
Doctor of Philosophy in Physics
Academic years 2012-2017



Acknowledgements

19 Ici on remerciera tous les gens que j'ai pu croiser durant cette aventure et qui m'ont
20 permis de passer un bon moment

21 *Gent, ici la super date de la mort qui tue de la fin d'écriture*
22 *Alexis Fagot*

Table of Contents

24	Acknowledgements	i
25	Nederlandse samenvatting	xv
26	English summary	xvii
27	1 Introduction	1-1
28	1.1 A story of High Energy Physics	1-1
29	1.2 Organisation of this study	1-1
30	2 Investigating the TeV scale	2-1
31	2.1 The Standard Model of Particle Physics	2-1
32	2.2 The Large Hadron Collider and the Compact Muon Solenoid . . .	2-1
33	2.3 Muon Phase-II Upgrade	2-1
34	3 Amplification processes in gaseous detectors	3-1
35	3.1 Signal formation	3-1
36	3.2 Gas transport parameters	3-1
37	4 Resistive Plate Chambers	4-1
38	4.1 Principle	4-1
39	4.2 Rate capability of Resistive Plate Chambers	4-1
40	4.3 High time resolution	4-1
41	4.4 Resistive Plate Chambers at CMS	4-1
42	5 Longevity studies and Consolidation of the present CMS RPC subsys-	5-1
43	tem	
44	5.1 Testing detectors under extreme conditions	5-1
45	5.1.1 High Luminosity LHC	5-1
46	5.1.2 The Gamma Irradiation Facilities	5-2
47	5.1.2.1 GIF	5-2
48	5.1.2.2 GIF++	5-3
49	5.2 Preliminary tests at GIF	5-5
50	5.2.1 Resistive Plate Chamber test setup	5-5
51	5.2.2 Data Acquisition	5-6
52	5.2.3 Geometrical acceptance of the setup layout to cosmic muons	5-7

53	5.2.3.1	Description of the simulation layout	5-8
54	5.2.3.2	Simulation procedure	5-10
55	5.2.3.3	Results	5-13
56	5.2.4	Photon flux at GIF	5-13
57	5.2.4.1	Expectations from simulations	5-13
58	5.2.4.2	Dose measurements	5-15
59	5.3	Longevity tests at GIF++	5-16
60	5.3.1	Description of the Data Acquisition	5-18
61	5.3.1.1	GIF++ RPC DAQ	5-22
62	5.3.1.2	RPC current, environmental and operation pa- rameter monitoring	5-23
63	5.3.2	Tools & Measurements	5-23
64	5.4	Results and discussions	5-23
65	5.4.1	Preliminary studies results	5-23
66	5.4.2	Longevity studies results	5-24
67			
68	6	Investigation on high rate RPCs	6-1
69	6.1	Rate limitations and ageing of RPCs	6-1
70	6.1.1	Low resistivity electrodes	6-1
71	6.1.2	Low noise front-end electronics	6-1
72	6.2	Construction of prototypes	6-1
73	6.3	Results and discussions	6-1
74	7	Conclusions and outlooks	7-1
75	7.1	Conclusions	7-1
76	7.2	Outlooks	7-1
77	A	A data acquisition software for VME CAEN TDCs	A-1
78	A.1	Introduction	A-1
79	B	Details on the online analysis package	B-1
80	B.1	Introduction	B-1
81	C	Structure of the hybrid simulation software	C-1
82	C.1	Introduction	C-1

List of Figures

84	2.1	Absorbed dose in the CMS cavern after an integrated luminosity	
85		of 3000 fb. R is the transverse distance from the beamline and Z is	
86		the distance along the beamline from the Interaction Point at Z=0.	2-2
87	2.2	A quadrant of the muon system, showing DTs (yellow), RPCs	
88		(light blue), and CSCs (green). The locations of new forward	
89		muon detectors for Phase-II are contained within the dashed box	
90		and indicated in red for GEM stations (ME0, GE1/1, and GE2/1)	
91		and dark blue for improved RPC (iRPC) stations (RE3/1 and RE4/1).	2-3
92	2.3	RMS of the multiple scattering displacement as a function of muon	
93		p_T for the proposed forward muon stations. All of the electromag-	
94		netic processes such as bremsstrahlung and magnetic field effect	
95		are included in the simulation.	2-3
96	5.1	Figure 5.1a represent the RPC rate measured in 2016 in p - p colli-	
97		sion runs as function of the instantaneous luminosity. Every point	
98		corresponds to a particular run. Figure 5.1b represent the inte-	
99		grated charge for Endcap. The integrated charge in years is shown	
100		in blue. The red curve shows the cumulative evolution of the inte-	
101		grated charge in time.	5-3
102	5.2	Layout of the test beam zone called X5c GIF at CERN. Photons	
103		from the radioactive source produce a sustained high rate of ran-	
104		dom hits over the whole area. The zone is surrounded by 8 m high	
105		and 80 cm thick concrete walls. Access is possible through three	
106		entry points. Two access doors for personnel and one large gate	
107		for material. A crane allows installation of heavy equipment in the	
108		area.	5-4
109	5.3	^{137}Cs decays by β^- emission to the ground state of ^{137}Ba (BR =	
110		5.64%) and via the 662 keV isomeric level of ^{137}Ba (BR = 94.36%)	
111		whose half-life is 2.55 min.	5-4

112	5.4	Description of the RPC setup. Dimensions are given in mm. Figure 5.4a provides a side view of the setup while Figure 5.4b shows a top view. A tent containing RPCs is placed at 1720 mm from the source container. The source is situated in the center of the container. RE-4-2-BARC-161 chamber is 160 mm inside the tent. This way, the distance between the source and the chambers plan is 2060 mm.	5-5
113			
114			
115			
116			
117			
118			
119	5.5	RE-4-2-BARC-161 chamber is inside the tent as described in Figure 5.4. In the top right, the two scintillators used as trigger can be seen. This trigger system has an inclination of 10° relative to horizontal and is placed above half-partition B2 of the RPCs. PMT electronics are shielded thanks to lead blocks placed in order to protect them without stopping photons from going through the scintillators and the chamber.	5-6
120			
121			
122			
123			
124			
125			
126	5.6	Hit distributions over all 3 partitions of RE-4-2-BARC-161 chamber is showed on these plots. Top, middle and bottom figures respectively correspond to partitions A, B, and C. These plots show that some events still occur in other half-partitions than B2, which corresponds to strips 49 to 64, in front of which the trigger is placed, contributing to the inefficiency of detection of cosmic muons. In the case of partitions A and C, the very low amount of data can be interpreted as noise. On the other hand, it is clear that a little portion of muons reach the half-partition B1, corresponding to strips 33 to 48.	5-7
127			
128			
129			
130			
131			
132			
133			
134			
135			
136	5.7	Signals from the RPC strips are shaped by the FEE described on Figure 5.7a. Output LVDS signals are then read-out by a TDC module connected to a computer or converted into NIM and sent to scalers. Figure 5.7b describes how these converted signals are put in coincidence with the trigger.	5-8
137			
138			
139			
140			
141	5.8	Description of the principle of a CFD. A comparison of threshold triggering (left) and constant fraction triggering (right) is shown in Figure 5.8a. Constant fraction triggering is obtained thanks to zero-crossing technique as explained in Figure 5.8b. The signal arriving at the input of the CFD is split into three components. A first one is delayed and connected to the inverting input of a first comparator. A second component is connected to the noninverting input of this first comparator. A third component is connected to the noninverting input of another comparator along with a threshold value connected to the inverting input. Finally, the output of both comparators is fed through an AND gate.	5-9
142			
143			
144			
145			
146			
147			
148			
149			
150			
151			

152	5.9	Results are derived from data taken on half-partition B2 only. On	
153		the 18 th of June 2014, data has been taken on chamber RE-2-	
154		BARC-161 at building 904 (Prevessin Site) with cosmic muons	
155		providing us a reference efficiency plateau of $(97.54 \pm 0.15)\%$ rep-	
156		resented by a black curve. A similar measurement has been done	
157		at GIF on the 21 st of July with the same chamber giving a plateau	
158		of $(78.52 \pm 0.94)\%$ represented by a red curve.	5-10
159	5.10	Representation of the layout used for the simulations of the test	
160		setup. The RPC is represented as a yellow trapezoid while the two	
161		scintillators as blue cuboids looking at the sky. A green plane cor-	
162		responds to the muon generation plane within the simulation. Fig-	
163		ure 5.4a shows a global view of the simulated setup. Figure 5.4b	
164		shows a zoomed view that allows to see the 2 scintillators as well	
165		as the full RPC plane.	5-11
166	5.11	γ flux $F(D)$ is plot using values from table 5.1. As expected, the	
167		plot shows similar attenuation behaviours with increasing distance	
168		for each absorption factors.	5-14
169	5.12	Figure 5.12a shows the linear approximation fit done via formul-	
170		ae 5.7 on data from table 5.2. Figure 5.12b shows a comparison	
171		of this model with the simulated flux using a and b given in fig-	
172		ure 5.12a in formulae 5.4 and the reference value $D_0 = 50cm$	
173		and the associated flux for each absorption factor F_0^{ABS} from ta-	
174		ble 5.1	5-16
175	5.13	Dose measurements has been done in a plane corresponding to the	
176		tents front side. This plan is 1900 mm away from the source. As	
177		explained in the first chapter, a lens-shaped lead filter provides a	
178		uniform photon flux in the vertical plan orthogonal to the beam	
179		direction. If the second line of measured fluxes is not taken into	
180		account because of lower values due to experimental equipments	
181		in the way between the source and the tent, the uniformity of the	
182		flux is well showed by the results.	5-17
183	5.14	Evolution of the maximum efficiency for RE2 (5.14a) and RE4	
184		(5.14b) chambers with increasing extrapolated γ rate per unit area	
185		at working point. Both irradiated (blue) and non irradiated (red)	
186		chambers are shown.	5-19
187	5.15	Evolution of the working point for RE2 (5.15a) and RE4 (5.15b)	
188		with increasing extrapolated γ rate per unit area at working point.	
189		Both irradiated (blue) and non irradiated (red) chambers are shown.	5-19
190	5.16	Evolution of the maximum efficiency at HL-LHC conditions, i.e.	
191		a background hit rate per unit area of 300 Hz/cm^2 , with increasing	
192		integrated charge for RE2 (5.16a) and RE4 (5.16b) detectors. Both	
193		irradiated (blue) and non irradiated (red) chambers are shown. The	
194		integrated charge for non irradiated detectors is recorded during	
195		test beam periods and stays small with respect to the charge accu-	
196		culated in irradiated chambers.	5-20

197	5.17	Comparison of the efficiency sigmoid before (triangles) and after	
198		(circles) irradiation for RE2 (5.17a) and RE4 (5.17b) detectors.	
199		Both irradiated (blue) and non irradiated (red) chambers are shown.	5-20
200	5.18	Evolution of the Bakelite resistivity for RE2 (5.18a) and RE4 (5.18b)	
201		detectors. Both irradiated (blue) and non irradiated (red) chambers	
202		are shown.	5-21
203	5.19	Evolution of the noise rate per unit area for the irradiated chamber	
204		RE2-2-BARC-9 only.	5-21
205	5.20	5-23

List of Tables

207	5.1	Total photon flux ($E\gamma \leq 662$ keV) with statistical error predicted	
208		considering a ^{137}Cs activity of 740 GBq at different values of the	
209		distance D to the source along the x-axis of irradiation field [6]. . .	5-13
210	5.2	Correction factor c is computed thanks to formulae 5.5 taking as	
211		reference $D_0 = 50$ cm and the associated flux F_0^{ABS} for each ab-	
212		sorption factor available in table 5.1.	5-14
213	5.3	The data at D_0 in 1997 is taken from [6]. In a second step, using	
214		Equations 5.8 and 5.9, the flux at D can be estimated in 1997.	
215		Then, taking into account the attenuation of the source activity,	
216		the flux at D can be estimated at the time of the tests in GIF in	
217		2014. Finally, assuming a sensitivity of the RPC to γ $s = 2 \cdot 10^{-3}$,	
218		an estimation of the hit rate per unit area is obtained.	5-17

List of Acronyms

List of Acronyms

B

225 BARC

Bhabha Atomic Research Centre

226 BR

Branching Ratio

C

231 CAEN

Costruzioni Apparecchiature Elettroniche Nucleari S.p.A.

233 CERN

European Organization for Nuclear Research

234 CFD

Constant Fraction Discriminator

235 CMS

Compact Muon Solenoid

236 CSC

Cathode Strip Chamber

D

241 DAQ

Data Acquisition

242 DCS

Detector Control Software

243 DQM

Data Quality Monitoring

244 DT

Drift Tube

F

249 FEE

Front-End Electronics

250	FEB	Front-End Board
251		
252		
253	G	
254		
255	GE-/-	Find a good description
256	GE1/1	Find a good description
257	GE2/1	Find a good description
258	GEANT	GEometry ANd Tracking - a series of software toolkit platforms developed by CERN
259		
260	GEM	Gas Electron Multiplier
261	GIF	old Gamma Irradiation Facility dismantled in 2014
262	GIF++	new Gamma Irradiation Facility
263		
264		
265	H	
266		
267	HL-LHC	High Luminosity LHC
268	HV	High Voltage
269		
270		
271	I	
272		
273	iRPC	improved RPC
274		
275		
276	L	
277		
278	LHC	Large Hadron Collider
279	LS1	First Long Shutdown
280	LS3	Third Long Shutdown
281	LV	Low Voltage
282	LVDS	Low-Voltage Differential Signaling
283		
284		
285	M	
286		
287	MC	Monte Carlo

288	MCNP	Monte Carlo N-Particle
289	ME-/-	Find good description
290	ME0	Find good description
291		
292		
293	N	
294		
295	NIM	Nuclear Instrumentation Module logic signals
296		
297		
298	P	
299		
300	PMT	PhotoMultiplier Tube
301		
302		
303	R	
304		
305	RE-/-	Find a good description
306	RE2/2	Find a good description
307	RE3/1	Find a good description
308	RE3/2	Find a good description
309	RE4/1	Find a good description
310	RE4/2	Find a good description
311	RE4/3	Find a good description
312	RMS	Root Mean Square
313	ROOT	a framework for data processing born at CERN
314	RPC	Resistive Plate Chamber
315		
316		
317	S	
318		
319	SPS	Super Proton Synchrotron
320		
321		
322	T	
323		
324	TDC	Time-to-Digital Converter

326

Nederlandse samenvatting –Summary in Dutch–

327

328 Le resume en Neerlandais (j'aurais peut-etre de apprendre la langue juste pour
329 ca...).

English summary

331 Le meme résumé mais en Anglais (on commencera par la hein!).

1

Introduction

332

333

334 **1.1 A story of High Energy Physics**

335 **1.2 Organisation of this study**

2

Investigating the TeV scale

2.1 The Standard Model of Particle Physics

2.2 The Large Hadron Collider and the Compact Muon Solenoid

2.3 Muon Phase-II Upgrade

After the more than two years lasting First Long Shutdown (LS1), the Large Hadron Collider (LHC) delivered its very first Run-II proton-proton collisions early 2015. LS1 gave the opportunity to the LHC and to the its experiments to undergo upgrades. The accelerator is now providing collisions at center-of-mass energy of 13 TeV and bunch crossing rate of 40 MHz, with a peak luminosity exceeding its design value. During the first and upcoming second LHC Long Shutdown, the Compact Muon Solenoid (CMS) detector is also undergoing a number of upgrades to maintain a high system performance [1].

From the LHC Phase-2 or High Luminosity LHC (HL-LHC) period onwards, i.e. past the Third Long Shutdown (LS3), the performance degradation due to integrated radiation as well as the average number of inelastic collisions per bunch crossing, or pileup, will rise substantially and become a major challenge for the LHC experiments, like CMS that are forced to address an upgrade program for Phase-II [2]. Simulations of the expected distribution of absorbed dose in the CMS detector under HL-LHC conditions, show in figure 5.13 that detectors placed close

to the beamline will have to withstand high irradiation, the radiation dose being of the order of a few tens of Gy.

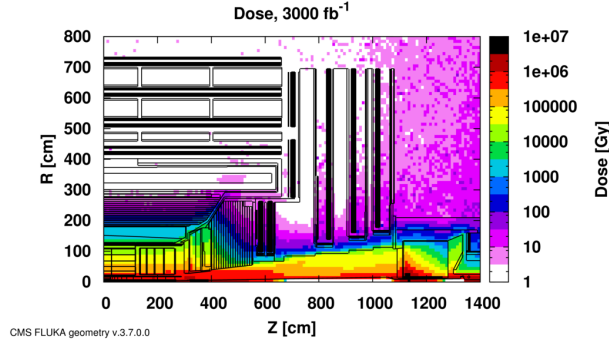


Figure 2.1: Absorbed dose in the CMS cavern after an integrated luminosity of 3000 fb. R is the transverse distance from the beamline and Z is the distance along the beamline from the Interaction Point at $Z=0$.

The measurement of small production cross-section and/or decay branching ratio processes, such as the Higgs boson coupling to charge leptons or the $B_s \rightarrow \mu^+ \mu^-$ decay, is of major interest and specific upgrades in the forward regions of the detector will be required to maximize the physics acceptance on the largest possible solid angle. To ensure proper trigger performance within the present coverage, the muon system will be completed with new chambers. In figure 2.2 one can see that the existing Cathode Strip Chambers (CSCs) will be completed by Gas Electron Multipliers (GEMs) and Resistive Plate Chambers (RPCs) in the pseudorapidity region $1.6 < |\eta| < 2.4$ to complete its redundancy as originally scheduled in the CMS Technical Proposal [3].

RPCs are used by the CMS first level trigger for their good timing performances. Indeed, a very good bunch crossing identification can be obtained with the present CMS RPC system, given their fast response of the order of 1 ns. In order to contribute to the precision of muon momentum measurements, muon chambers should have a spatial resolution less or comparable to the contribution of multiple scattering [1]. Most of the plausible physics is covered only considering muons with $p_T < 100$ GeV thus, in order to match CMS requirements, a spatial resolution of $\mathcal{O}(\text{few mm})$ the proposed new RPC stations, as shown by the simulation in figure 2.3. According to preliminary designs, RE3/1 and RE4/1 readout pitch will be comprised between 3 and 6 mm and 5 η -partitions could be considered.

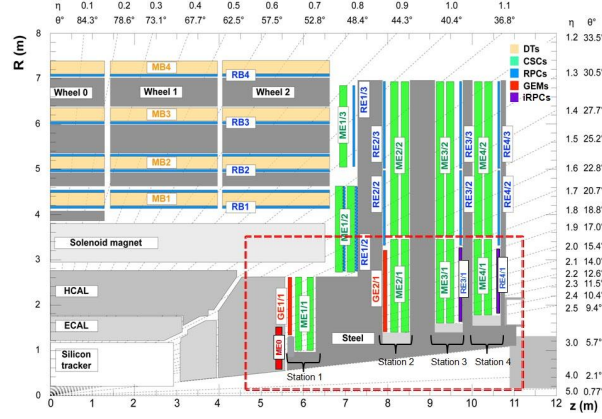


Figure 2.2: A quadrant of the muon system, showing DTs (yellow), RPCs (light blue), and CSCs (green). The locations of new forward muon detectors for Phase-II are contained within the dashed box and indicated in red for GEM stations (ME0, GE1/1, and GE2/1) and dark blue for improved RPC (iRPC) stations (RE3/1 and RE4/1).

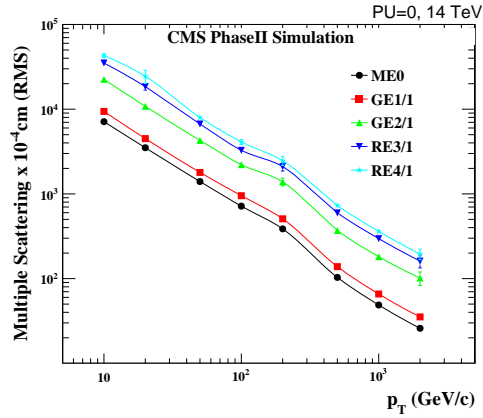


Figure 2.3: RMS of the multiple scattering displacement as a function of muon p_T for the proposed forward muon stations. All of the electromagnetic processes such as bremsstrahlung and magnetic field effect are included in the simulation.

3

379

380

Amplification processes in gaseous detectors

381

382

3.1 Signal formation

383

3.2 Gas transport parameters

4

384

385

Resistive Plate Chambers

386 **4.1 Principle**

387 **4.2 Rate capability of Resistive Plate Chambers**

388 **4.3 High time resolution**

389 **4.4 Resistive Plate Chambers at CMS**

5

390

391 Longevity studies and Consolidation of 392 the present CMS RPC subsystem

393 5.1 Testing detectors under extreme conditions

394 5.1.1 High Luminosity LHC

395 The upgrade from LHC to HL-LHC will increase the peak luminosity from 10^{34}
396 $\text{cm}^{-2} \text{s}^{-1}$ to reach $7.5 \times 10^{34} \text{ cm}^{-2} \text{s}^{-1}$, increasing in the same way the total ex-
397 pected background to which the RPC system will be subjected to. Composed of
398 low energy gammas and neutrons from p - p collisions, low momentum primary
399 and secondary muons, punch-through hadrons from calorimeters, and particles pro-
400 duced in the interaction of the beams with collimators, the background will mostly
401 affect the regions of CMS that are the closest to the beam line, i.e. the RPC detec-
402 tors located in the endcaps.

403 The information collected with 2016 data allowed us to understand that the hottest
404 RPC regions are located in the fourth endcap stations. Extrapolating from the
405 data shown in Figure 5.1, the maximum rate per unit area under HL-LHC condi-
406 tions is therefore foreseen to increase to values of the order of 400 Hz/cm^2 in the
407 chambers of the present muon system. To the 4000 fb^{-1} of integrated luminosity,
408 over the 10 years of HL-LHC lifetime, will correspond $\sim 0.4 \text{ C/cm}^2$ of integrated
409 charge inside the hottest regions of the detectors, considering the current total de-
410 livered luminosity from p - p collisions of about 75 fb^{-1} and the total integrated
411 charge estimated to be about 5.8 mC/cm^2 in the endcap.

During Run-I, the RPC system provided stable operation and excellent performance and did not show any aging effects. In the past, extensive long-term tests were carried out at several gamma and neutron facilities certifying the detector performance up to values of dose, charge and fluence close to those expected after ten years of HL-LHC operation. Both full size and small prototype RPCs have been irradiated with photons up to an integrated charge of $\sim 0.05 \text{ C/cm}^2$ and $\sim 0.4 \text{ C/cm}^2$, respectively [4, 5].

In this perspective, studying the performance of the present system up to an integrated charge of $\sim 1.2 \text{ C/cm}^2$, 3 times higher than what expected for 10 years of operation of HL-LHC, and background hit rates of 1200 Hz/cm^2 , 3 times stronger than what expected from the designed peak luminosity, and identifying possible long-term aging effects are necessary steps to take to insure that the RPCs will be able to cope with the high radiation conditions.

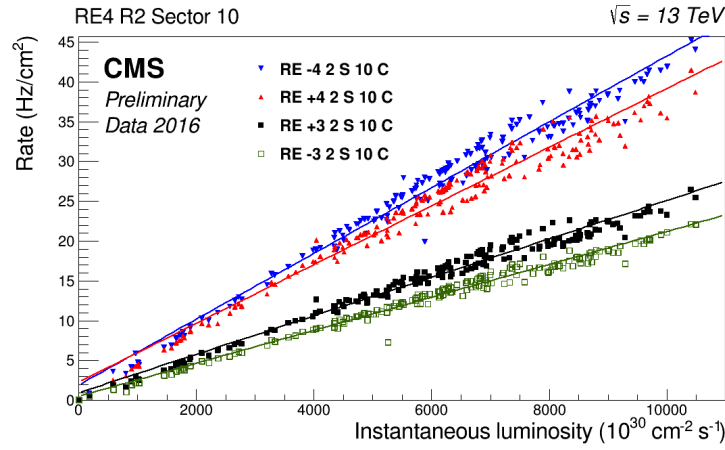
5.1.2 The Gamma Irradiation Facilities

5.1.2.1 GIF

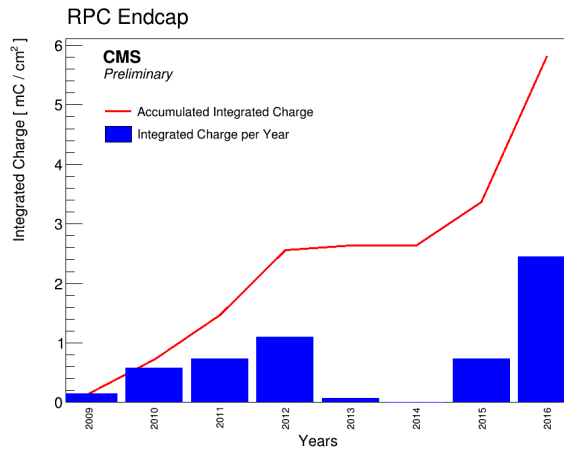
GIF was a test area located in the SPS West Area at the downstream end of the X5 test beam in which particle detectors were exposed to a particle beam in presence of an adjustable background flux of photons [**GIF** facility]. This facility's goal was to simulate background conditions these detectors would suffer in their operating environment at the LHC. A schematic layout of the GIF zone is shown in Figure 5.2. Photons are produced by a strong radioactive source of ^{137}Cs installed in the upstream part of the zone inside a lead container, which includes a collimator, designed to irradiate a $6 \times 6 \text{ m}^2$ area at 5 m distance from the source. A thin lens-shaped lead filter renders the outcoming flux uniform in the vertical plane orthogonal to the beam direction. Control of the photon rate is achieved by further lead filters allowing the maximum rate to be limited and to vary within a range of four orders of magnitude. The γ source is located in a rectangular lead container.

As described on Figure 5.3, the ^{137}Cs source with a half-life of 30 years and an activity of 740 GBq, as measured on the 5th March 1997, emits a 662 keV photon in 85% of the decays. The principal collimator hole provides a pyramidal aperture of $74^\circ \times 74^\circ$ solid angle. This provides a photon flux in a pyramidal volume of 5 m maximum length along the beam axis.

Particle detectors under test are then placed within the pyramidal volume in front of the source, perpendicularly to the beam line in order to profit from the homogeneous photon flux. Adjusting the background flux of photons can then be done by using the filters and choosing the position of the detectors with respect to the source.



(a)



(b)

Figure 5.1: Figure 5.1a represent the RPC rate measured in 2016 in p - p collision runs as function of the instantaneous luminosity. Every point corresponds to a particular run. Figure 5.1b represent the integrated charge for Endcap. The integrated charge in years is shown in blue. The red curve shows the cumulative evolution of the integrated charge in time.

5.1.2.2 GIF++

GIF++ is a test area located in the SPS North Area at the downstream end of the H4 test beam. In this facility, particle detectors are tested using a particle beam in presence of an adjustable background flux of photons. The goal is to simulate background conditions these detectors would suffer in their operating

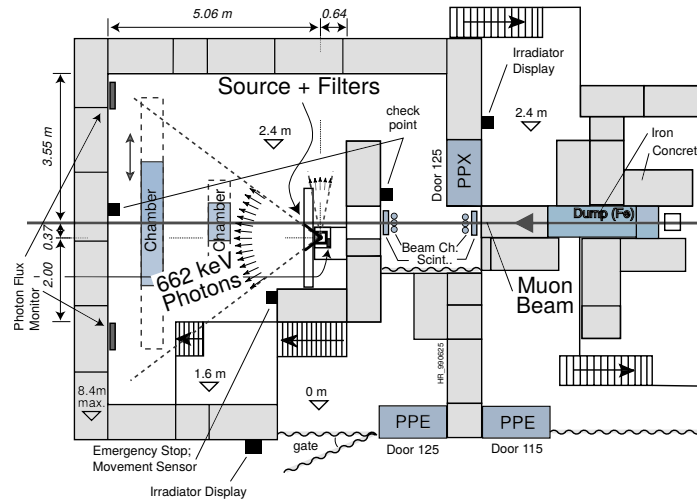


Figure 5.2: Layout of the test beam zone called X5c GIF at CERN. Photons from the radioactive source produce a sustained high rate of random hits over the whole area. The zone is surrounded by 8 m high and 80 cm thick concrete walls. Access is possible through three entry points. Two access doors for personnel and one large gate for material. A crane allows installation of heavy equipment in the area.

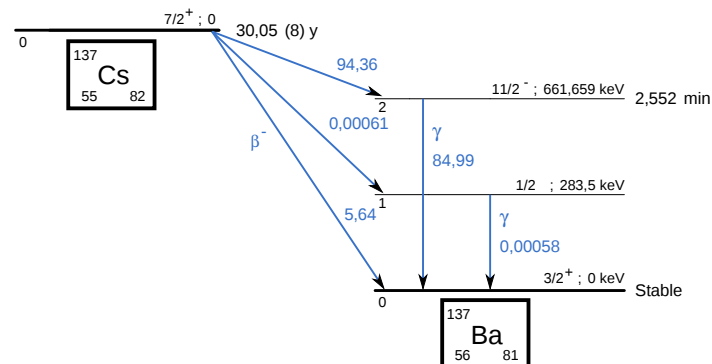


Figure 5.3: ^{137}Cs decays by β^- emission to the ground state of ^{137}Ba ($BR = 5.64\%$) and via the 662 keV isomeric level of ^{137}Ba ($BR = 94.36\%$) whose half-life is 2.55 min.

environment at the HL-LHC. Gamma photons are produced by a strong radioactive ^{137}Cs source installed in the center part of the zone, with an activity of 13.1 TBq, emitting 662 keV photons. A thin lens-shaped lead filter renders the outcoming flux uniform in the vertical plane orthogonal to the beam direction. Control of the photon rate is achieved by using a set of filters allowing the maximum rate to be

461 limited and to vary within a range of four orders of magnitude. The H4 beam,
462 composed of muons with a momentum of about 150 GeV/c, passes through the
463 GIF++ zone and is used to study the performance of the detectors. Its flux is of
464 104 particles/s/cm² focused in an area similar to 10 × 10 cm².

465 5.2 Preliminary tests at GIF

466 5.2.1 Resistive Plate Chamber test setup

467 During summer 2014, preliminary tests have been conducted in the GIF area on
468 a newly produced RE4/2 chamber labelled RE-4-2-BARC-161. This chamber has
469 been placed into a trolley covered with a tent. The position of the RPC inside the
470 tent and of the tent related to the source is described in Figure 5.4. To test this
471 CMS RPC, three different absorber settings were used. First of all, measurements
472 were done with fully opened source. Then, to complete this preliminary study, the
473 gamma flux has been attenuated by a factor 2 and a factor 5. The expected gamma
474 flux at the level of our detector will be discussed in subsection 5.2.4.

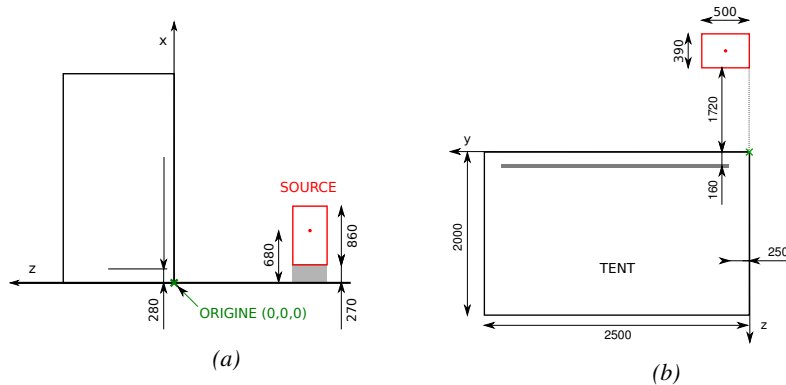


Figure 5.4: Description of the RPC setup. Dimensions are given in mm. Figure 5.4a provides a side view of the setup while Figure 5.4b shows a top view. A tent containing RPCs is placed at 1720 mm from the source container. The source is situated in the center of the container. RE-4-2-BARC-161 chamber is 160 mm inside the tent. This way, the distance between the source and the chambers plan is 2060 mm.

475 At the time of the tests, the beam not being operationnal anymore, a trigger
476 composed of 2 plastic scintillators has been placed in front of the setup with an
477 inclination of 10 deg (*this has to be first confirmed by the simulation - I will ad-*
478 *just in consequence cause it has never been precisely measured*) with respect to
479 the detector plane in order to look at cosmic muons. Using this particular trig-
480 ger layout, shown on Figure 5.5, leads to a cosmic muon hit distribution into the
481 chamber similar to the one in Figure 5.6. Measured without gamma irradiation,

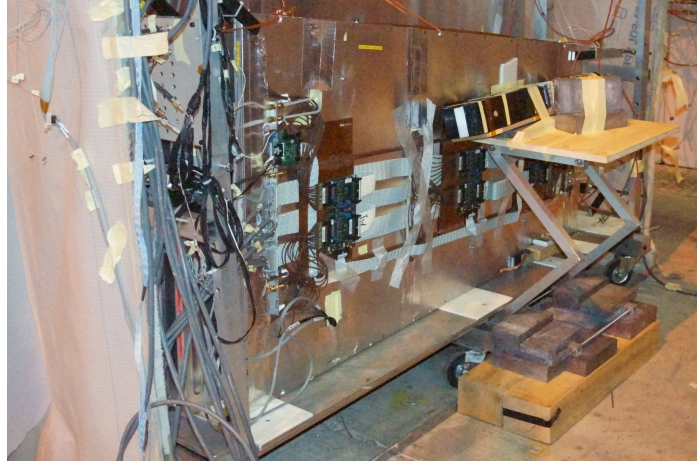


Figure 5.5: RE-4-2-BARC-161 chamber is inside the tent as described in Figure 5.4. In the top right, the two scintillators used as trigger can be seen. This trigger system has an inclination of 10° relative to horizontal and is placed above half-partition B2 of the RPCs. PMT electronics are shielded thanks to lead blocks placed in order to protect them without stopping photons from going through the scintillators and the chamber.

482 two peaks can be seen on the profil of partition B, centered on strips 52 and 59.
 483 Sub-section 5.2.3 will help us understand that these two peaks are due respectively
 484 to forward and backward coming cosmic particles where forward coming particles
 485 are first detected by the scintillators and then the RPC while the backward coming
 486 muons are first detected in the RPC.

487 5.2.2 Data Acquisition

488 Signals induced by cosmic particle in the RPC strips are shaped by standard CMS
 489 RPC Front-End Electronics (FEE) following the scheme of Figure 5.7. On a first
 490 stage, analogic signals are amplified and then sent to the Constant Fraction Dis-
 491 criminator (CFD) described in Figure 5.8. At the end of the chain, 100 ns long
 492 pulses are sent in the LVDS output. These output signal are sent on one side to a
 493 V1190A Time-to-Digital Converter (TDC) module from CAEN and on the other
 494 to an OR module to count the number of detected signals. Trigger and hit coinci-
 495 dences are monitored using scalers. The TDC is used to store the data into ROOT
 496 files. These files are thus analysed to understand the detectors performance.

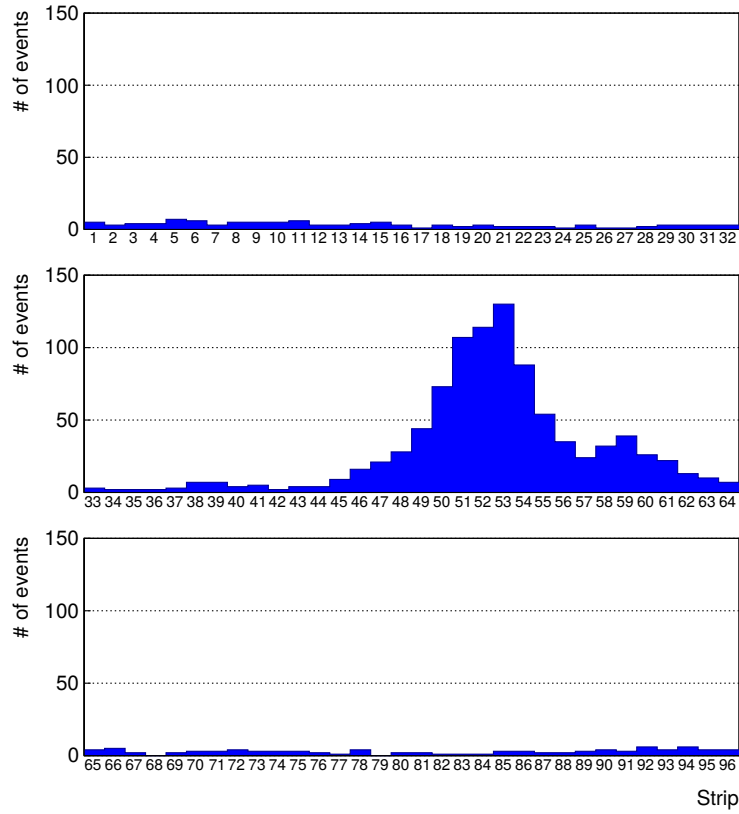
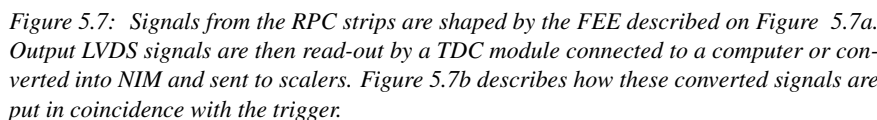


Figure 5.6: Hit distributions over all 3 partitions of RE-4-2-BARC-161 chamber is showed on these plots. Top, middle and bottom figures respectively correspond to partitions A, B, and C. These plots show that some events still occur in other half-partitions than B2, which corresponds to strips 49 to 64, in front of which the trigger is placed, contributing to the inefficiency of detection of cosmic muons. In the case of partitions A and C, the very low amount of data can be interpreted as noise. On the other hand, it is clear that a little portion of muons reach the half-partition B1, corresponding to strips 33 to 48.

5.2.3 Geometrical acceptance of the setup layout to cosmic muons

In order to profit from a constant gamma irradiation, the detectors inside of the GIF bunker need to be placed in a plane orthogonal to the beam line. The muon beam that used to be available was meant to test the performance of detectors under test. This beam not being active anymore, another solution to test detector performance had to be used. Thus, it has been decided to use cosmic muons detected through a telescope composed of two scintillators. Lead blocks were used as shielding to

515 **5.2.3.1 Description of the simulation layout**

The layout of GIF setup has been reproduced and incorporated into a Monte Carlo (MC) simulation to study the influence of the disposition of the telescope on the final distribution measured by the RPC. A 3D view of the simulated layout is given into Figure 5.10. Muons are generated randomly in a horizontal plane located at a height corresponding to the lowest point of the PMTs. This way, the needed size of the plane in order to simulate events happening at very big azimuthal angles (i.e. $\theta \approx \pi$) can be kept relatively small. The muon flux is designed to follow the usual

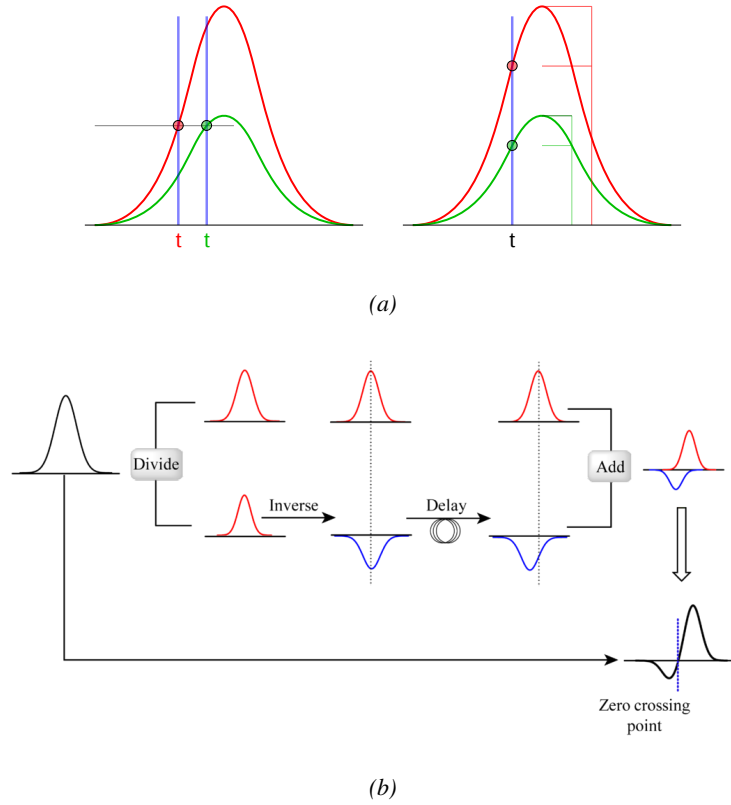


Figure 5.8: Description of the principle of a CFD. A comparison of threshold triggering (left) and constant fraction triggering (right) is shown in Figure 5.8a. Constant fraction triggering is obtained thanks to zero-crossing technique as explained in Figure 5.8b. The signal arriving at the input of the CFD is split into three components. A first one is delayed and connected to the inverting input of a first comparator. A second component is connected to the noninverting input of this first comparator. A third component is connected to the noninverting input of another comparator along with a threshold value connected to the inverting input. Finally, the output of both comparators is fed through an AND gate.

523 $\cos^2\theta$ distribution for cosmic particle. The goal of the simulation is to look at
 524 muons that pass through the muon telescope composed of the two scintillators and
 525 define their distribution onto the RPC plane. During the reconstruction, the RPC
 526 plane is then divided into its strips and each muon track is assigned to a strip.

527 In order to further refine the quality of the simulation and understand deeper
 528 the results the dependance of the distribution has been studied for a range of tele-
 529 scope inclinations. Moreover, the threshold applied on the PMT signals has been
 530 included into the simulation in the form of a cut. In the approximation of uni-

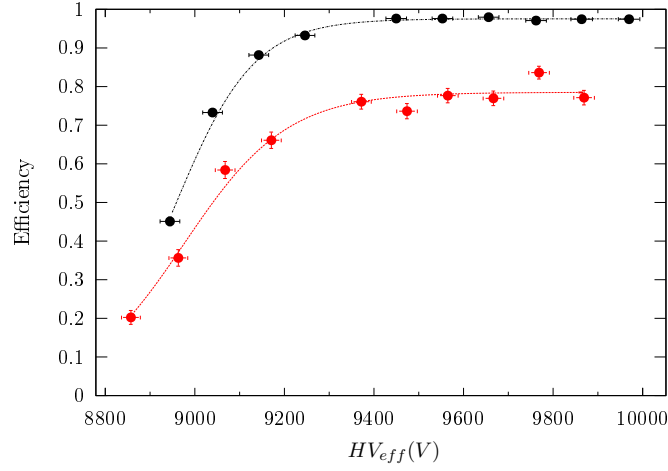


Figure 5.9: Results are derived from data taken on half-partition B2 only. On the 18th of June 2014, data has been taken on chamber RE-2-BARC-161 at building 904 (Prevessin Site) with cosmic muons providing us a reference efficiency plateau of $(97.54 \pm 0.15)\%$ represented by a black curve. A similar measurement has been done at GIF on the 21st of July with the same chamber giving a plateau of $(78.52 \pm 0.94)\%$ represented by a red curve.

form scintillators, it has been considered that the threshold can be understood as the minimum distance particles need to travel through the scintillating material to give a strong enough signal. Particles that travel a distance smaller than the set "threshold" are thus not detected by the telescope and cannot trigger the data taking. Finally, the FEE threshold also has been considered in a similar way. The mean momentum of horizontal cosmic rays is higher than those of vertical ones but the stopping power of matter for momenta ranging from 1 GeV to 1 TeV stays comparable. It is then possible to assume that the mean number of primary e^- /ion pairs per unit length will stay similar and thus, depending on the applied discriminator threshold, muons with the shortest path through the gas volume will deposit less charge and induce a smaller signal on the pick-up strips that could eventually not be detected. These two thresholds also restrain the overall geometrical acceptance of the system.

5.2.3.2 Simulation procedure

The simulation software has been designed using C++ and the output data is saved into ROOT histograms. Simulations start for a threshold T_{scint} varying in a range from 0 to 45 mm in steps of 5 mm, where $T_{scint} = 0$ mm corresponds to the case

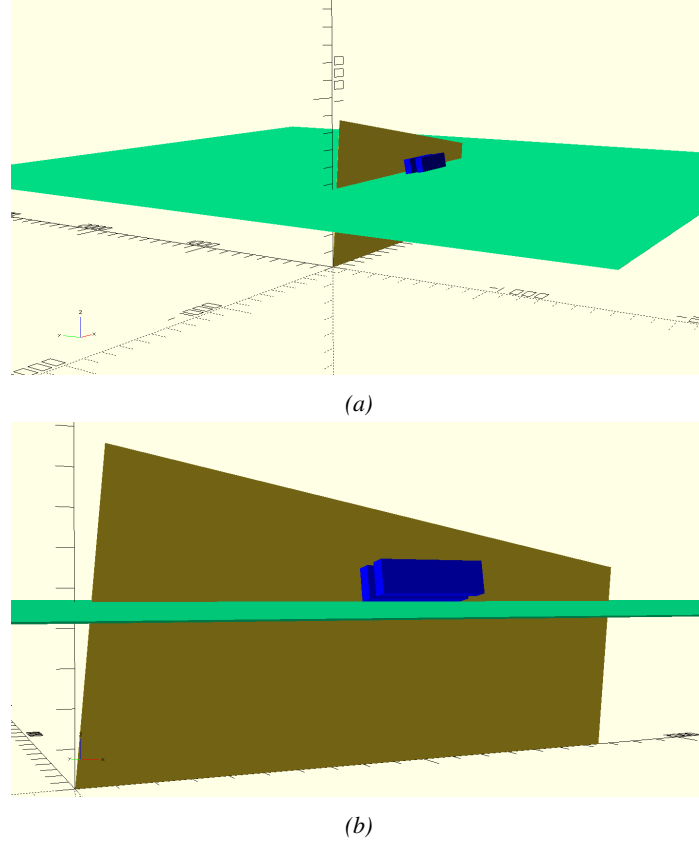


Figure 5.10: Representation of the layout used for the simulations of the test setup. The RPC is represented as a yellow trapezoid while the two scintillators as blue cuboids looking at the sky. A green plane corresponds to the muon generation plane within the simulation. Figure 5.4a shows a global view of the simulated setup. Figure 5.4b shows a zoomed view that allows to see the 2 scintillators as well as the full RPC plane.

where there isn't any threshold apply on the input signal while $T_{scint} = 45$ mm, which is the scintillator thickness, is the case where muons cannot arrive orthogonally onto the scintillator surface. For a given T_{scint} , a set of RPC thresholds are considered. The RPC threshold, T_{RPC} varies from 2 mm, the thickness of the gas volume, to 3 mm in steps of 0.25 mm. For each $(T_{scint}; T_{RPC})$ pair, $N_{\mu} = 10^8$ muons are randomly generated inside the muon plane described in the previous paragraph with an azimuthal angle θ chosen to follow a $\cos^2\theta$ distribution.

Planes are associated to each surface of the scintillators. Knowing muon position into the muon plane and its direction allows us, by assuming that muons travel in a straight line, to compute the intersection of the muon track with these planes.

558 Applying conditions to the limits of the surfaces of the scintillator faces then gives
 559 us an answer to whether or not the muon passed through the scintillators. In the
 560 case the muon has indeed passed through the telescope, the path through each scin-
 561 tillator is computed and muons whose path was shorter than T_{scint} are rejected and
 562 are thus considered as having not interacted with the setup.

563 On the contrary, if the muon is labeled as good, its position within the RPC
 564 plane is computed and the corresponding strip, determined by geometrical tests
 565 in the case the distance through the gas volume was enough not to be rejected
 566 because of T_{RPC} , gets a hit and several histograms are filled in order to keep
 567 track of the generation point on the muon plane, the intersection points of the
 568 reconstructed muons within the telescope, or on the RPC plane, the path traveled
 569 through each individual scintillator or the gas volume, as well as other histograms.
 570 Moreover, muons fill different histograms whether they are forward or backward
 571 coming muons. They are discriminated according to their direction components.
 572 When a muon is generated, an (x, y, z) position is assigned into the muon plane as
 573 well as a $(\theta; \phi)$ pair that gives us the direction it's coming from. This way, muons
 574 satisfying the condition $0 \leq \phi < \pi$ are designated as backward coming muons
 575 while muons satisfying $\pi \leq \phi < 2\pi$ as forward coming muons.

576 This simulation is then repeated for different telescope inclinations ranging in
 577 between 4 and 20° and varying in steps of 2° . Due to this inclination and to the
 578 vertical position of the detector under test, the muon distribution reconstructed in
 579 the detector plane is asymmetrical. The choice has been made to choose a skew
 580 distribution formula to fit the data built as the multiplication of gaussian and sig-
 581 moidal curves together. A typical gaussian formula is given as 5.1 and has three
 582 free parameters as A_g , its amplitude, \bar{x} , its mean value and σ , its root mean square.
 583 Sigmoidal curves as given by formula 5.2 are functions converging to 0 and A_s as
 584 x diverges. The inflexion point is given as x_i and λ is proportional to the slope at
 585 $x = x_i$. In the limit where $\lambda \rightarrow \infty$, the sigmoid becomes a step function.

$$g(x) = A_g e^{\frac{-(x-\bar{x})^2}{2\sigma^2}} \quad (5.1)$$

$$s(x) = \frac{A_s}{1 + e^{-\lambda(x-x_i)}} \quad (5.2)$$

586 Finally, a possible representation of a skew distribution is given by formula 5.3
 587 and is the product of 5.1 and 5.2. Naturally, here $A_{sk} = A_g \times A_s$ and represents
 588 the theoretical maximum in the limit where the skew tends to a gaussian function.

$$sk(x) = g(x) \times s(x) = A_{sk} \frac{e^{\frac{-(x-\bar{x})^2}{2\sigma^2}}}{1 + e^{-\lambda(x-x_i)}} \quad (5.3)$$

589 **5.2.3.3 Results**

590 **Influence of T_{scint} on the muon distribution**

591 **Influence of T_{RPC} on the muon distribution**

592 **Influence of the telescope inclination on the muon distribution**

593 **Comparison to data taken at GIF without irradiation**

594 **5.2.4 Photon flux at GIF**

595 **5.2.4.1 Expectations from simulations**

596 In order to understand and evaluate the γ flux in the GIF area, simulations had been
 597 conducted in 1999 and published by S. Agosteo et al [6]. Table 5.1 presented in
 598 this article gives us the γ flux for different distances D to the source. This sim-
 599 ulation was done using GEANT and a Monte Carlo N-Particle (MCNP) transport
 600 code, and the flux F is given in number of γ per unit area and unit time along with
 601 the estimated error from these packages expressed in %.

Nominal ABS	Photon flux F [$\text{s}^{-1}\text{cm}^{-2}$]			
	at $D = 50$ cm	at $D = 155$ cm	at $D = 300$ cm	at $D = 400$ cm
1	$0.12 \cdot 10^8 \pm 0.2\%$	$0.14 \cdot 10^7 \pm 0.5\%$	$0.45 \cdot 10^6 \pm 0.5\%$	$0.28 \cdot 10^6 \pm 0.5\%$
2	$0.68 \cdot 10^7 \pm 0.3\%$	$0.80 \cdot 10^6 \pm 0.8\%$	$0.25 \cdot 10^6 \pm 0.8\%$	$0.16 \cdot 10^6 \pm 0.6\%$
5	$0.31 \cdot 10^7 \pm 0.4\%$	$0.36 \cdot 10^6 \pm 1.2\%$	$0.11 \cdot 10^6 \pm 1.2\%$	$0.70 \cdot 10^5 \pm 0.9\%$

Table 5.1: Total photon flux ($E\gamma \leq 662$ keV) with statistical error predicted considering a ^{137}Cs activity of 740 GBq at different values of the distance D to the source along the x -axis of irradiation field [6].

602 The simulation doesn't directly provides us with an estimated flux at the level
 603 of our RPC. First of all, it is needed to extract the value of the flux from the
 604 available data contained in the original paper and then to estimate the flux in 2014
 605 at the time the experimentation took place. Figure 5.11 that contains the data from
 606 Table 5.1. In the case of a pointlike source emitting isotrope and homogeneous
 607 gamma radiations, the gamma flux F at a distance D to the source with respect
 608 to a reference point situated at D_0 where a known flux F_0 is measured will be
 609 expressed like in Equation 5.4, assuming that the flux decreases as $1/D^2$, where c
 610 is a fitting factor.

$$F^{ABS} = F_0^{ABS} \times \left(\frac{cD_0}{D} \right)^2 \quad (5.4)$$

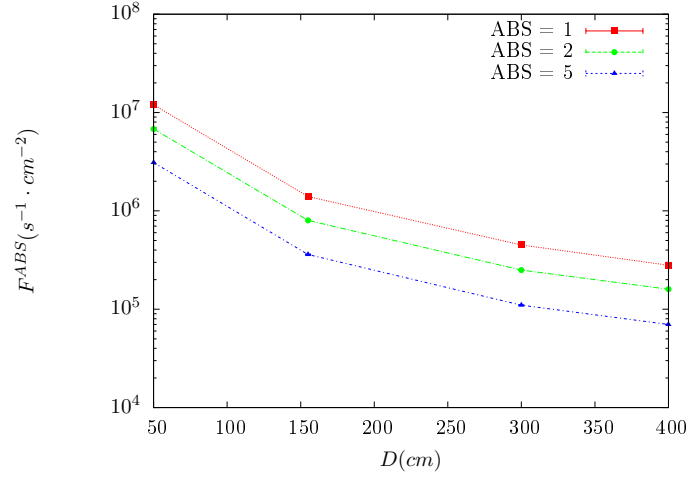


Figure 5.11: γ flux $F(D)$ is plot using values from table 5.1. As expected, the plot shows similar attenuation behaviours with increasing distance for each absorption factors.

By rewriting Equation 5.4, it comes that :

$$c = \frac{D}{D_0} \sqrt{\frac{F^{ABS}}{F_0^{ABS}}} \quad (5.5)$$

$$\Delta c = \frac{c}{2} \left(\frac{\Delta F^{ABS}}{F^{ABS}} + \frac{\Delta F_0^{ABS}}{F_0^{ABS}} \right) \quad (5.6)$$

Finally, using Equation 5.5 and the data in Table 5.1 with $D_0 = 50$ cm as reference point, we can build Table 5.2. It is interesting to note that c for each value of D doesn't depend on the absorption factor.

Nominal ABS	Correction factor c		
	at $D = 155$ cm	at $D = 300$ cm	at $D = 400$ cm
1	$1.059 \pm 0.70\%$	$1.162 \pm 0.70\%$	$1.222 \pm 0.70\%$
2	$1.063 \pm 1.10\%$	$1.150 \pm 1.10\%$	$1.227 \pm 0.90\%$
5	$1.056 \pm 1.60\%$	$1.130 \pm 1.60\%$	$1.202 \pm 1.30\%$

Table 5.2: Correction factor c is computed thanks to formulae 5.5 taking as reference $D_0 = 50$ cm and the associated flux F_0^{ABS} for each absorption factor available in table 5.1.

For the range of D/D_0 values available, it is possible to use a simple linear fit to get the evolution of c . The linear fit will then use only 2 free parameters, a

617 and b , as written in Equation 5.7. This gives us the results showed in Figure 5.12.
 618 Figure 5.12b confirms that using only a linear fit to extract c is enough as the
 619 evolution of the rate that can be obtained superimposes well on the simulation
 620 points.

$$c \left(\frac{D}{D_0} \right) = a \frac{D}{D_0} + b \quad (5.7)$$

$$F^{ABS} = F_0^{ABS} \left(a + \frac{bD_0}{D} \right)^2 \quad (5.8)$$

$$\Delta F^{ABS} = F^{ABS} \left[\frac{\Delta F_0^{ABS}}{F_0^{ABS}} + 2 \frac{\Delta a + \Delta b \frac{D_0}{D}}{a + \frac{bD_0}{D}} \right] \quad (5.9)$$

621 In the case of the 2014 GIF tests, the RPC plane is located at a distance
 622 $D = 206$ cm to the source. Moreover, to estimate the strength of the flux in 2014,
 623 it is necessary to consider the nuclear decay through time associated to the Cesium
 624 source whose half-life is well known ($t_{1/2} = (30.05 \pm 0.08)$ y). The very first
 625 source activity measurement has been done on the 5th of March 1997 while the
 626 GIF tests were done in between the 20th and the 31st of August 2014, i.e. at a
 627 time $t = (17.47 \pm 0.02)$ y resulting in an attenuation of the activity from 740 GBq
 628 in 1997 to 494 GBq in 2014. All the needed information to extrapolate the flux
 629 through our detector in 2014 has now been assembled, leading to the Table 5.3. It
 630 is interesting to note that for a common RPC sensitivity to γ of $2 \cdot 10^{-3}$, the order
 631 of magnitude of the estimated hit rate per unit area is of the order of the kHz for
 632 the fully opened source. Moreover, taking profit of the two working absorbers, it
 633 will be possible to scan background rates at 0 Hz, ~ 300 Hz as well as ~ 600 Hz.
 634 Without source, a good estimate of the intrinsic performance will be available.
 635 Then at 300 Hz, the goal will be to show that the detectors fulfill the performance
 636 certification of CMS RPCs. Then a first idea of the performance of the detectors at
 637 higher background will be provided with absorption factors 2 (~ 600 Hz) and 1 (no
 638 absorption). *[Here I will also put a reference to the plot showing the estimated*
 639 *background rate at the level of RE3/1 in the case of HL-LHC but this one being*
 640 *in another chapter, I will do it later.]*

641 5.2.4.2 Dose measurements

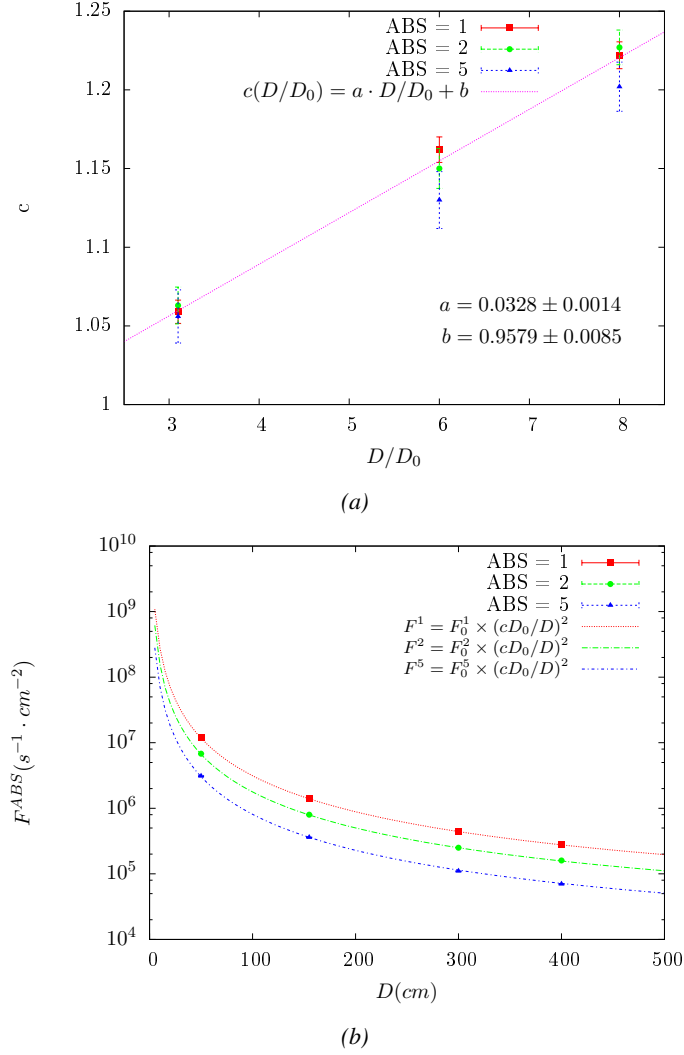


Figure 5.12: Figure 5.12a shows the linear approximation fit done via formulae 5.7 on data from table 5.2. Figure 5.12b shows a comparison of this model with the simulated flux using a and b given in figure 5.12a in formulae 5.4 and the reference value $D_0 = 50cm$ and the associated flux for each absorption factor F_0^{ABS} from table 5.1

5.3 Longevity tests at GIF++

This study implies a monitoring of the performance of the detectors probed using a high intensity muon beam in a irradiated environment by periodically measuring their rate capability, the dark current running through them and the bulk resistivity

Nominal ABS	Photon flux F [$s^{-1}cm^{-2}$]			Hit rate/unit area [$Hz\ cm^{-2}$] at $D^{2014} = 206\ cm$
	at $D_0^{1997} = 50\ cm$	at $D^{1997} = 206\ cm$	at $D^{2014} = 206\ cm$	
1	$0.12 \cdot 10^8 \pm 0.2\%$	$0.84 \cdot 10^6 \pm 0.3\%$	$0.56 \cdot 10^6 \pm 0.3\%$	1129 ± 32
2	$0.68 \cdot 10^7 \pm 0.3\%$	$0.48 \cdot 10^6 \pm 0.3\%$	$0.32 \cdot 10^6 \pm 0.3\%$	640 ± 19
5	$0.31 \cdot 10^7 \pm 0.4\%$	$0.22 \cdot 10^6 \pm 0.3\%$	$0.15 \cdot 10^6 \pm 0.3\%$	292 ± 9

Table 5.3: The data at D_0 in 1997 is taken from [6]. In a second step, using Equations 5.8 and 5.9, the flux at D can be estimated in 1997. Then, taking into account the attenuation of the source activity, the flux at D can be estimated at the time of the tests in GIF in 2014. Finally, assuming a sensitivity of the RPC to $\gamma\ s = 2 \cdot 10^{-3}$, an estimation of the hit rate per unit area is obtained.

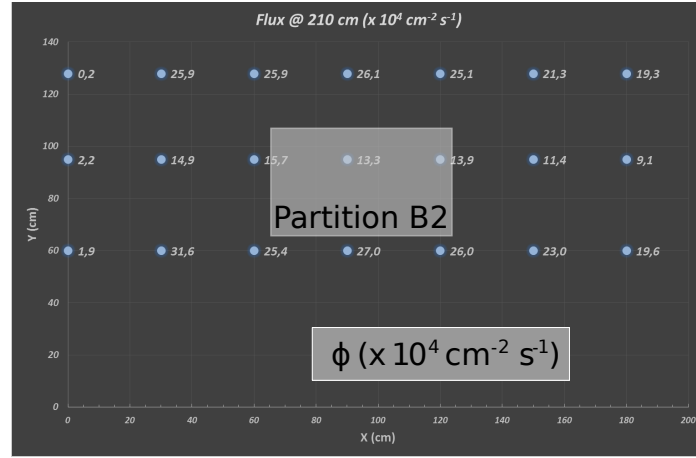


Figure 5.13: Dose measurements has been done in a plane corresponding to the tents front side. This plan is 1900 mm away from the source. As explained in the first chapter, a lens-shaped lead filter provides a uniform photon flux in the vertical plan orthogonal to the beam direction. If the second line of measured fluxes is not taken into account because of lower values due to experimental equipments in the way between the source and the tent, the uniformity of the flux is well showed by the results.

646 of the Bakelite composing their electrodes. GIF++, with its very intense ^{137}Cs
647 source, provides the perfect environment to perform such kind of tests. Assuming
648 a maximum acceleration factor of 3, it is expected to accumulate the equivalent
649 charge in 1.7 years.
650 As the maximum background is found in the endcap, the choice naturally was
651 made to focus the GIF++ longevity studies on endcap chambers. Most of the RPC
652 system was installed in 2007. Nevertheless, the large chambers in the fourth end-
653 cap (RE4/2 and RE4/3) have been installed during LS1 in 2014. The Bakelite of
654 these two different productions having different properties, four spare chambers

of the present system were selected, two RE2,3/2 spares and two RE4/2 spares. Having two chambers of each type allows to always keep one of them non irradiated as reference, the performance evolution of the irradiated chamber being then compared through time to the performance of the non irradiated one.

The performance of the detectors under different level of irradiation is measured periodically during dedicated test beam periods using the H4 muon beam. In between these test beam periods, the two RE2,3/2 and RE4/2 chambers selected for this study are irradiated by the ^{137}Cs source in order to accumulate charge and the gamma background is monitored, as well as the currents. The two remaining chambers are kept non-irradiated as reference detectors. Due to the limited gas flow in GIF++, the RE4 chamber remained non-irradiated until end of November 2016 where a new mass flow controller has been installed allowing for bigger volumes of gas to flow in the system.

Figures 5.14 and 5.15 give us for different test beam periods, and thus for increasing integrated charge through time, a comparison of the maximum efficiency, obtained using a sigmoid-like function, and of the working point of both irradiated and non irradiated chambers [7]. No aging is yet to see from this data, the shifts in γ rate per unit area in between irradiated and non irradiated detectors and RE2 and RE4 types being easily explained by a difference of sensitivity due to the various Bakelite resistivities of the HPL electrodes used for the electrode production.

Collecting performance data at each test beam period allows us to extrapolate the maximum efficiency for a background hit rate of 300 Hz/cm^2 corresponding to the expected HL-LHC conditions. Aging effects could emerge from a loss of efficiency with increasing integrated charge over time, thus Figure 5.16 helps us understand such degradation of the performance of irradiated detectors in comparison with non irradiated ones. The final answer for an eventual loss of efficiency is given in Figure 5.17 by comparing for both irradiated and non irradiated detectors the efficiency sigmoids before and after the longevity study. Moreover, to complete the performance information, the Bakelite resistivity is regularly measured thanks to Ag scans (Figure 5.18) and the noise rate is monitored weekly during irradiation periods (Figure 5.19). At the end of 2016, no signs of aging were observed and further investigation is needed to get closer to the final integrated charge requirements proposed for the longevity study of the present CMS RPC sub-system.

5.3.1 Description of the Data Acquisition

For the longevity studies, four spare chambers of the present system are used. Two spare RPCs of the RE2,3 stations as well as two spare RPCs from the new RE4 stations have been mounted in a Trolley. Six RE4 gaps are also placed in the trolley. The trolley is placed inside the GIF++ in the upstream region of the bunker,

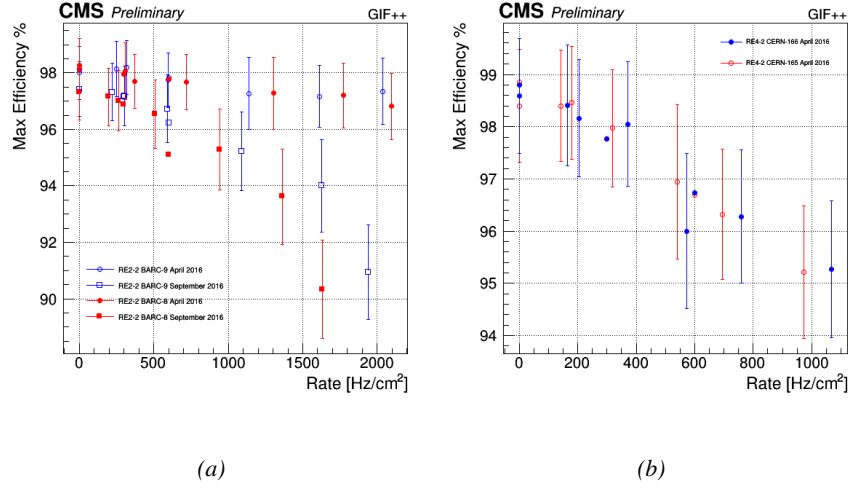


Figure 5.14: Evolution of the maximum efficiency for RE2 (5.14a) and RE4 (5.14b) chambers with increasing extrapolated γ rate per unit area at working point. Both irradiated (blue) and non irradiated (red) chambers are shown.

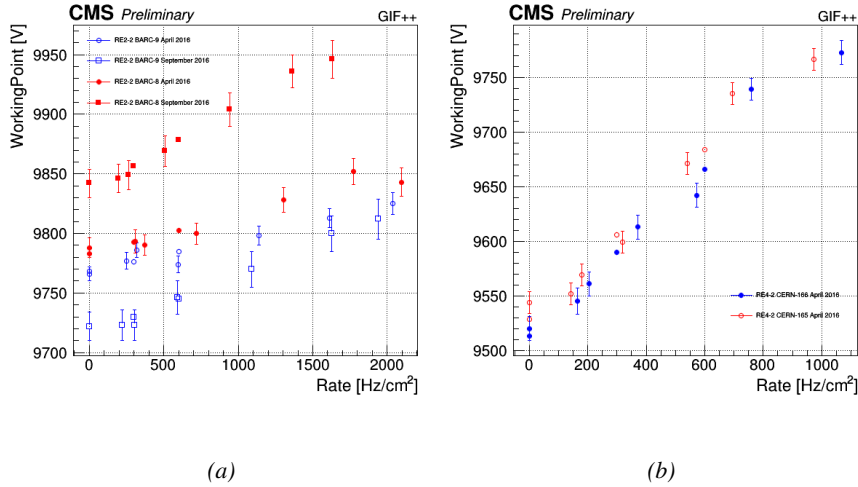


Figure 5.15: Evolution of the working point for RE2 (5.15a) and RE4 (5.15b) with increasing extrapolated γ rate per unit area at working point. Both irradiated (blue) and non irradiated (red) chambers are shown.

694 taking the cesium source as a reference. The trolley is oriented for the detection
 695 surface of the chambers to be orthogonal to the beam line. The system can be
 696 moved along the orthogonal plane in order to have the beam in all η -partitions.

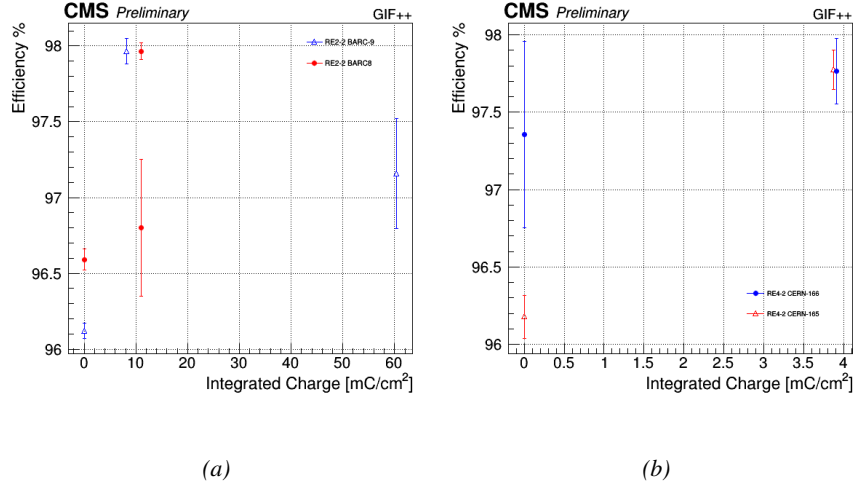


Figure 5.16: Evolution of the maximum efficiency at HL-LHC conditions, i.e. a background hit rate per unit area of 300 Hz/cm², with increasing integrated charge for RE2 (5.16a) and RE4 (5.16b) detectors. Both irradiated (blue) and non irradiated (red) chambers are shown. The integrated charge for non irradiated detectors is recorded during test beam periods and stays small with respect to the charge accumulated in irradiated chambers.

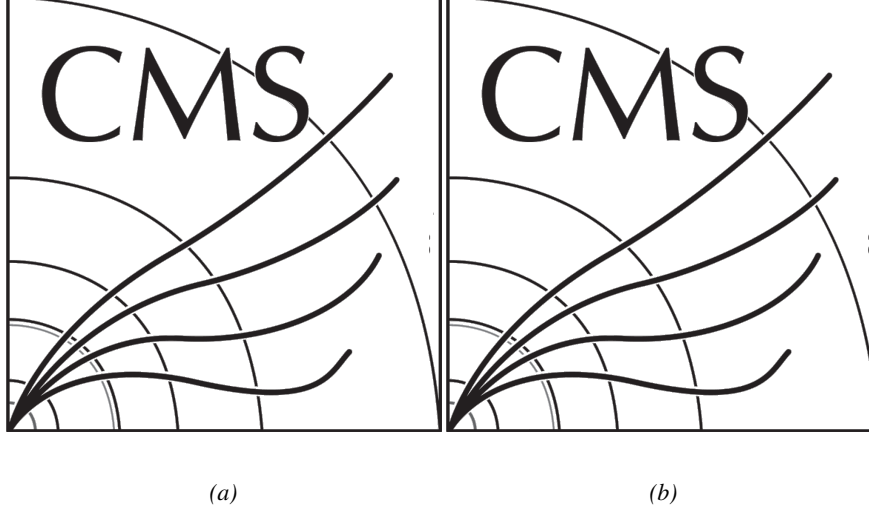


Figure 5.17: Comparison of the efficiency sigmoid before (triangles) and after (circles) irradiation for RE2 (5.17a) and RE4 (5.17b) detectors. Both irradiated (blue) and non irradiated (red) chambers are shown.

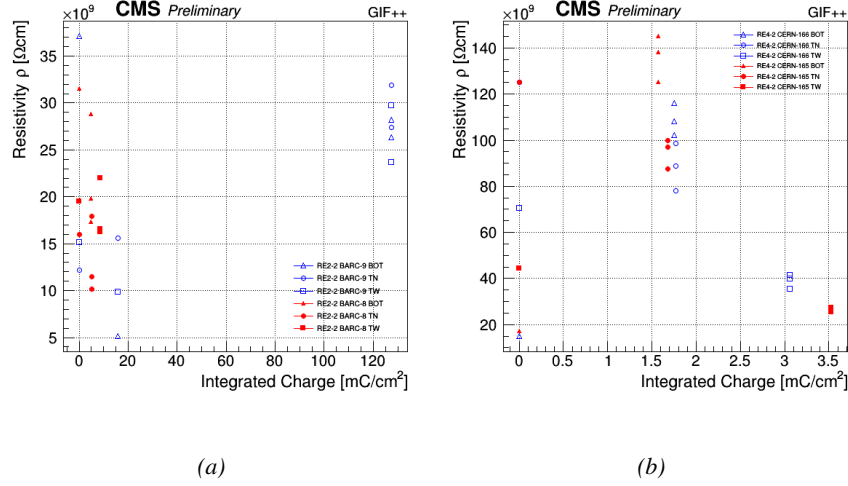


Figure 5.18: Evolution of the Bakelite resistivity for RE2 (5.18a) and RE4 (5.18b) detectors. Both irradiated (blue) and non irradiated (red) chambers are shown.

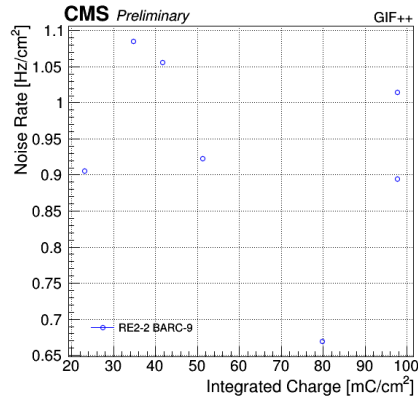


Figure 5.19: Evolution of the noise rate per unit area for the irradiated chamber RE2-2-BARC-9 only.

of 5.2 m to the source, which irradiates the bunker using an attenuation filter of 2.2 which corresponds to a fluence of 10^7 gamma/cm^2 .

During GIF++ operation, the data collected can be divided into different categories as several parameters are monitored in addition to the usual RPC performance data. On one hand, to know the performance of a chamber, it is need to measure its efficiency and to know the background conditions in which it is operated. To do this, the hit signals from the chamber are recorded and stored in a

ROOT file via a Data Acquisition (DAQ) software. On the other hand, it is also very important to monitor parameters such as environmental pressure and temperature, gas temperature and humidity, RPC HV, LV, and currents, or even source and beam status. This is done through the GIF++ web Detector Control Software (DCS) that stores this information in a database.

5.3.1.1 GIF++ RPC DAQ

Two different types of tests are conducted on RPCs via the DAQ. Indeed, the performance of the detectors is measured periodically during dedicated test beam periods using the H4 muon beam. In between these test beam periods, when the beam is not available, the chambers are irradiated by the ^{137}Cs in order to accumulate deposited charge and the gamma background is measured.

RPCs under test are connected through LVDS cables to V1190A Time-to-Digital Converter (TDC) modules manufactured by CAEN. These modules, located in the rack area outside of the bunker, get the logic signals sent by the chambers and save them into their buffers. Due to the limited size of the buffers, the collected data is regularly erased and replaced. A trigger signal is needed for the TDC modules to send the useful data to the DAQ computer via a V1718 CAEN USB communication module.

In the case of performance test, the trigger signal used for data acquisition is generated by the coincidence of three scintillators. A first one is placed upstream outside of the bunker, a second one is placed downstream outside of the bunker, while a third one is placed in front of the trolley, close by the chambers. Every time a trigger is sent to the TDCs, i.e. every time a muon is detected, knowing the time delay in between the trigger and the RPC signals, signals located in the right time window are extracted from the buffers and saved for later analysis. Signals are taken in a time window of 400 ns centered on the muon peak (here we could show a time spectrum). On the other hand, in the case of background rate measurement, the trigger signal needs to be "random" not to measure muons but to look at gamma background. A trigger pulse is continuously generated at a rate of 300 Hz using a dual timer. To integrate an as great as possible time, all signals contained within a time window of 10us prior to the random trigger signal are extracted from the buffers and saved for further analysis (here another time spectrum to illustrate could be useful, maybe even place both spectrum together as a single Figure).

The signals sent to the TDCs correspond to hit collections in the RPCs. When a particle hits a RPC, it induce a signal in the pickup strips of the RPC readout. If this signal is higher than the detection threshold, a LVDS signal is sent to the TDCs. The data is then organised into 4 branches keeping track of the event number, the hit multiplicity for the whole setup, and the time and channel profile of the hits in the TDCs.

5.3.1.2 RPC current, environmental and operation parameter monitoring

In order to take into account the variation of pressure and temperature between different data taking periods the applied voltage is corrected following the relationship :

$$HV_{eff} = HV_{app} \times \left(0.2 + 0.8 \cdot \frac{P_0}{P} \times \frac{T}{T_0} \right) \quad (5.10)$$

where T_0 (=293 K) and P_0 (=990 mbar) are the reference values.

5.3.2 Tools & Measurements

Insert a short description of the online tools (DAQ, DCS, DQM).

Insert a short description of the offline tools : tracking and efficiency algorithm.

Identify long term aging effects we are monitoring the rates per strip.

5.4 Results and discussions

5.4.1 Preliminary studies results

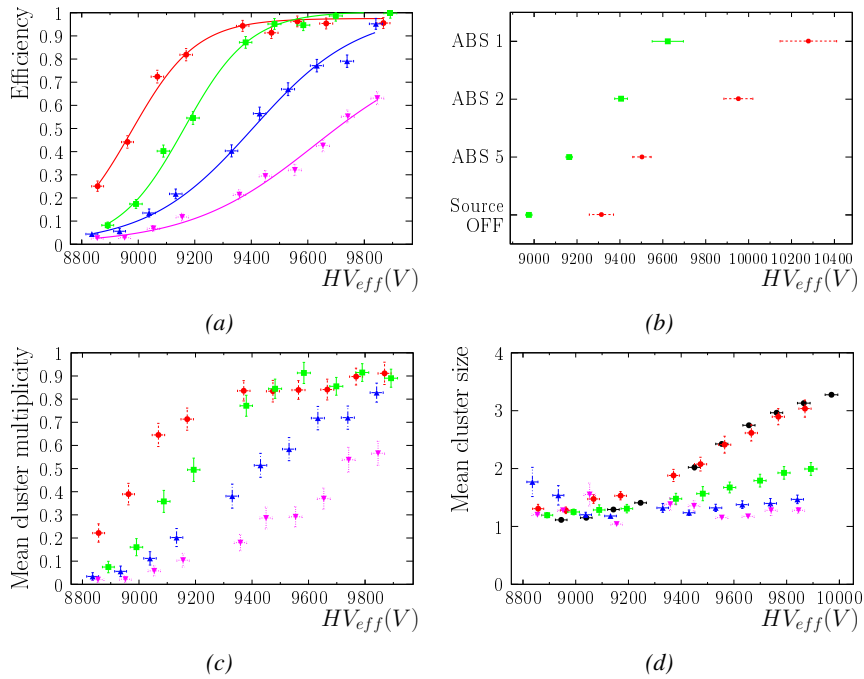


Figure 5.20

755 **5.4.2 Longevity studies results**

6

756

757

Investigation on high rate RPCs

758 **6.1 Rate limitations and ageing of RPCs**

759 **6.1.1 Low resistivity electrodes**

760 **6.1.2 Low noise front-end electronics**

761 **6.2 Construction of prototypes**

762 **6.3 Results and discussions**

7

763

764

Conclusions and outlooks

765 **7.1 Conclusions**

766 **7.2 Outlooks**

References

- [1] CERN. Geneva. LHC Experiments Committee. *The CMS muon project : Technical Design Report*. Tech. rep. CERN-LHCC-97-032. CMS Collaboration, 1997.
- [2] CERN. Geneva. LHC Experiments Committee. *Technical Proposal for the Phase-II Upgrade of the CMS Detector*. Tech. rep. CERN-LHCC-2015-010. CMS Collaboration, 2015.
- [3] CERN. Geneva. LHC Experiments Committee. *CMS, the Compact Muon Solenoid : technical proposal*. Tech. rep. CERN-LHCC-94-38. CMS Collaboration, 1994.
- [4] M. Abbrescia et al. “Study of long-term performance of CMS RPC under irradiation at the CERN GIF”. In: *NIMA* 533 (2004), pp. 102–106.
- [5] H.C. Kim et al. “Quantitative aging study with intense irradiation tests for the CMS forward RPCs”. In: *NIMA* 602 (2009), pp. 771–774.
- [6] S. Agosteo et al. “A facility for the test of large-area muon chambers at high rates”. In: *NIMA* 452 (2000), pp. 94–104.
- [7] M. Abbrescia et al. “Cosmic ray tests of double-gap resistive plate chambers for the CMS experiment”. In: *NIMA* 550 (2005), pp. 116–126.



785

786

787

A data acquisition software for VME CAEN TDCs

788

A.1 Introduction

789

Start text here...

B

790

791

Details on the online analysis package

792

B.1 Introduction

793

insert text here



794

795

796

Structure of the hybrid simulation software

797

C.1 Introduction

798

insert text here...

